Journal of Non-Crystalline Solids 387 (2014) 36–40

Contents lists available at ScienceDirect

Journal of Non-Crystalline Solids

journal homepage: www.elsevier.com/locate/jnoncrysol

Non-isothermal kinetic studies of crystallization in amorphous $Al_{86}Ni_{10}MM_4$ alloy

M. Mansouri [a], A. Simchi [a,b,*], J.I. Lee [c], E.S. Park [c], N. Varahram [a]

[a] Department of Materials Science and Engineering, Sharif University of Technology, 14588 Tehran, Iran
[b] Institute for Nanoscience and Nanotechnology, Sharif University of Technology, 14588 Tehran, Iran
[c] Research Institute of Advanced Materials, Department of Materials Science and Engineering, Seoul National University, Seoul 151-744, Republic of Korea

ARTICLE INFO

Article history:
Received 17 October 2013
Received in revised form 8 December 2013
Available online 11 January 2014

Keywords:
Amorphous aluminum alloy;
Kinetics;
Calorimetry;
Autocatalytic model;
Nano-indentation

ABSTRACT

$Al_{86}Ni_{10}MM_4$ (MM: Mischmetal) amorphous ribbons were prepared by melt spinning on a child copper wheel. Non-isothermal crystallization kinetics of the amorphous alloy was studied by differential scanning calorimetry (DSC). The crystallized phases were determined by X-ray diffraction method and transmission electron microscopy. DSC traces were analyzed by Kissinger method to determine the apparent activation energy of crystallization. Changes in the activation energy (E_α) with progression of crystallization were also evaluated by differential iso-conversional method of Friedman. For the precipitation of nanometer-sized Al particles, the activation energy slightly increased with increasing the conversion fraction up to $\alpha = 0.2$, but remained almost constant until $\alpha = 0.8$. Because of the solute enrichment around the particles in the matrix, higher values of E_α were obtained at the late stage of crystallization. Results of nano-indentation test also showed a significant improvement in the hardness of the ribbons due to the formation of fcc-Al nanoparticles.

1. Introduction

Al-based amorphous alloys containing rare-earth metals are commonly produced by rapid solidification. These metallic glasses have generated much interest for structural applications because of their promising mechanical properties combined with low density and high corrosion resistance [1–4]. Among various alloys, Al–Ni–RE system has been studied frequently due to high glass forming ability and good thermal stability [5–8].

Tensile strengths higher than 1000 MPa in amorphous phase [9] and up to 1500 MPa in partially crystallized state [10,11] have been reported. Inoue et al. [12] reported that crystallization of nano-metric Al particles suppresses shear sliding of the amorphous matrix. Therefore, controlled crystallization of amorphous Al alloys is essential to attain high mechanical properties. As a result, crystallization kinetics of these alloys has been studied frequently for more than a decade [13–15].

In the present study, the crystallization kinetics of nanometer-sized Al particles in melt-spun $Al_{86}Ni_{10}MM_4$ (MM: Mischmetal) ribbons has been investigated by isochronal differential scanning calorimetry (DSC) at different heating rates. Since the main constituent elements of MM (Ce, La, Nd, and Pr) have a negative heat of mixing with aluminum, it is expectable that glass forming ability is enhanced. On the other hand, MM is cheaper than elemental rare-earth metals, which is important for the production of Al-based amorphous alloys. However, due to the presence of several glass-forming elements, crystallization of MM-containing Al-based amorphous alloys is a complex process. Therefore, studies are required to evaluate the crystallization kinetics of MM-containing Al alloys. The aim of this paper is to investigate the formation of nano-metric Al particles upon devitrification of $Al_{86}Ni_{10}MM_4$ amorphous ribbons. DSC traces were recorded at different heating rates and analyzed by autocatalytic model [16]. Transmission electron microscopy (TEM) and X-ray diffraction (XRD) method were also utilized to determine the crystallized phases.

2. Materials and methods

2.1. Experimental procedure

Aluminum (99.99% and nickel (99.99%) rods (RND Korea, South Korea) were used as the starting materials. Cerium mischmetal with nominal composition of (at.%) 55 Ce, 25 La, 15 Nd, and 5 Pr with a purity of 99% was provided by RND Korea, South Korea. $Al_{86}Ni_{10}MM_4$ master alloy was prepared by arc melting under Ti-getter high purity argon atmosphere (99.999%). To insure the compositional homogeneity of the primary ingot, arc melting was afforded and the remelting was performed three times. The amorphous ribbons were prepared by a single-roll melt spinning machine operated in a partial argon atmosphere. The diameter of copper roll was 250 mm and the rotation speed was 3500 rpm. The average width and thickness of the prepared amorphous ribbons were 2.5 mm and 0.025 mm, respectively.

---

* Corresponding author at: Department of Materials Science and Engineering, Sharif University of Technology, 14588 Tehran, Iran. Tel.: +98 21 6616 5261; fax: +98 21 6600 5717.
E-mail address: simchi@sharif.edu (A. Simchi).

0022-3093/$ – see front matter © 2013 Elsevier B.V. All rights reserved.
http://dx.doi.org/10.1016/j.jnoncrysol.2013.12.027

XRD (New D8 Advance, Bruker, Germany) was utilized to evaluate the amorphous state of as-quenched ribbons and the crystallized phases. Monochromatic Cu Kα radiation in the range of $2\theta = 10$–$80°$ was utilized. Annealing of the amorphous ribbons was performed at a heating rate of 20 K/min at different temperatures of 553, 623 and 714 K in a differential scanning calorimeter (Perkin Elmer DSC-8, USA). After reaching the desired temperature, the temperature was rapidly decreased with a rate of ~150 K/min. The microstructure of the ribbons before and after annealing was examined by using a high-resolution TEM (JEOL 2100F HRTEM, Tokyo, Japan). Thin foils for HRTEM were prepared by Ar ion milling using Gatan (PIPS 691) at 2 eV with liquid nitrogen cooling. Thermal analyses at different heating rates were also performed by DSC under a high purity argon gas flow. The weight of the samples was ~10 mg and the utilized pan was aluminum. Two runs were performed for each sample. The second run serves as a base line.

In order to examine hardness of the ribbons in amorphous and annealed sate, nano-indentation test was afforded. Metallographic techniques were utilized to attain mirror smooth surfaces. A Tribolab nano-indentation system (Hysitron, Inc., Minneapolis, MN, USA) with Berkovich diamond tip was utilized. The load control mode (5000 μN) was afforded. On each sample, 25 indentations were carried out and the mean hardness values ± standard deviation were reported.

2.2. Kinetic theory

The reaction rate is commonly expressed as a function of temperature (T) and extent of conversion (α) as [17]:

$$\frac{d\alpha}{dt} = A\exp\left(\frac{-E}{RT}\right)f(\alpha) \tag{1}$$

where t represent time, A the pre-exponential factor, E the activation energy, R the gas constant, and $f(\alpha)$ a function that represents the reaction model. Various solid state reaction models [16–23] link $f(\alpha)$ to the reaction mechanism. In order to identify a proper model for a given system, the below characteristic functions can be utilized [18]:

$$z(\alpha) = \left(\frac{d\alpha}{dt}\right)T\left[\frac{\pi(x)}{\beta}\right] \tag{2}$$

$$y(\alpha) = \left(\frac{d\alpha}{dt}\right)\exp(x) \tag{3}$$

where β is the heating rate, $x = E/RT$, and $\pi(x)$ is a function of temperature integral and can be approximated by Senum-Yang equation [24]:

$$\pi(x) = \frac{x^3 + 18x^2 + 88x + 96}{x^4 + 20x^3 + 120x^2 + 240x + 120} \tag{4}$$

According to Kissinger method [19], the apparent activation energy of the crystallization can be related to the heating rate (β) and the peak temperature (T_p) in DSC traces by:

$$\ln\left(\frac{\beta}{RT_p^2}\right) = -\frac{E}{RT_p} + constant \tag{5}$$

The activation energy can also be evaluated by iso-conversional methods [20]. In the differential iso-conversional method of Friedman [21], the activation energy at a given conversion fraction (E_α) is expressed by the following equation:

$$\ln\left(\frac{d\alpha}{dt}\right)_\alpha = -\frac{E_\alpha}{RT_\alpha} + constant \tag{6}$$

where $(d\alpha/dt)_\alpha$ and T_α denote the specific reaction rate and temperature corresponding to fixed value of conversion (α), respectively. In order to determine the errors involved in the calculation of thermodynamics quantities, OriginPro 8.5.0 SR1 Software (OriginLab Corporation MA, USA) was utilized.

3. Results

Fig. 1 shows a typical DSC curve of the $Al_{86}Ni_{10}MM_4$ ribbon at a heating rate of 20 K/min. The existence of several exothermic peaks determines multi-stage crystallization process. XRD and TEM were utilized to evaluate the amorphous state of as-quenched ribbons and phases formed after thermal treatment. Fig. 2a shows XRD patterns of as-quenched and annealed $Al_{86}Ni_{10}MM_4$ ribbons at different temperatures. The as-quenched ribbon exhibited a broad diffusive pattern without any distinct crystalline peak. TEM study supported the XRD results, i.e. no crystalline phase was detected (Fig. 2b). The XRD pattern of the annealed ribbon at 518 K shows the characteristic peaks of fcc-Al particles. A bright-field TEM image of this sample is shown in Fig. 2c. Nanometer-sized aluminum clusters with an average size of 50 nm are seen. HRTEM image of the clusters is shown in Fig. 2d. The irregular clusters are composed of single crystals without parallel lattice fringes. Twin-like boundaries between domains reveal nucleation on the surface of the growing crystals. XRD patterns of the annealed ribbons at higher temperatures (623 K and 715 K) also show the formation of $Al_{11}MM_3$ and Al_3Ni phases (Fig. 2a). It should be noted that formation of these compounds should be avoided as hardness and fracture toughness decrease by depletion of the solute elements in the amorphous phase [3].

To gain an insight on the mechanical properties of the ribbons, nano-indentation test was performed. Fig. 3 shows the load-displacement curves. The hardness of the amorphous ribbon was 3.82 ± 0.10 GPa. After isochronal annealing at 553 K, the hardness value was 6.20 ± 0.17 GPa. The result indicates the prime role of the fcc-Al crystallization on the hardness of the amorphous ribbon.

To investigate the crystallization kinetics of the aluminum-based amorphous alloy containing MM, non-isothermal DSC experiments were performed at various heating rates. The DSC traces are shown in Fig. 4a. As seen, the temperature peaks are shifted to higher temperatures as the heating rate increases. This observation indicates that the crystallization is a thermal activated process [25]. The apparent activation energy of the first crystallization sequence can be determined by employing Kissinger method Eq.(5). Fig. 4b shows a plot of ln (β/T_p^2)

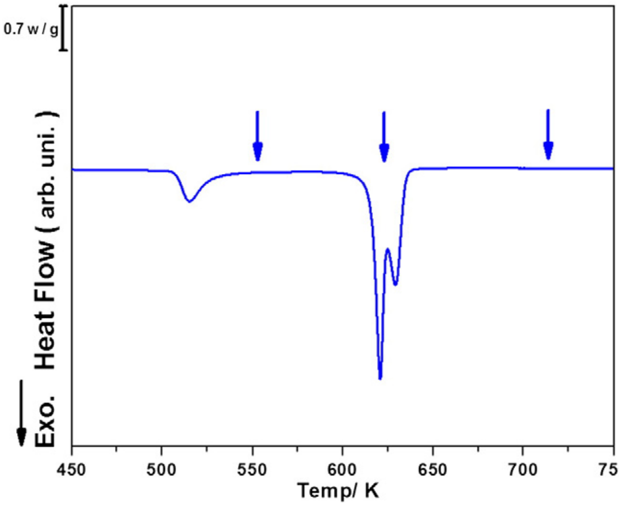

Fig. 1. DSC trace for $Al_{86}Ni_{10}MM_4$ ribbon at a heating rate of 20 K/min. The annealing temperatures are shown by arrow.

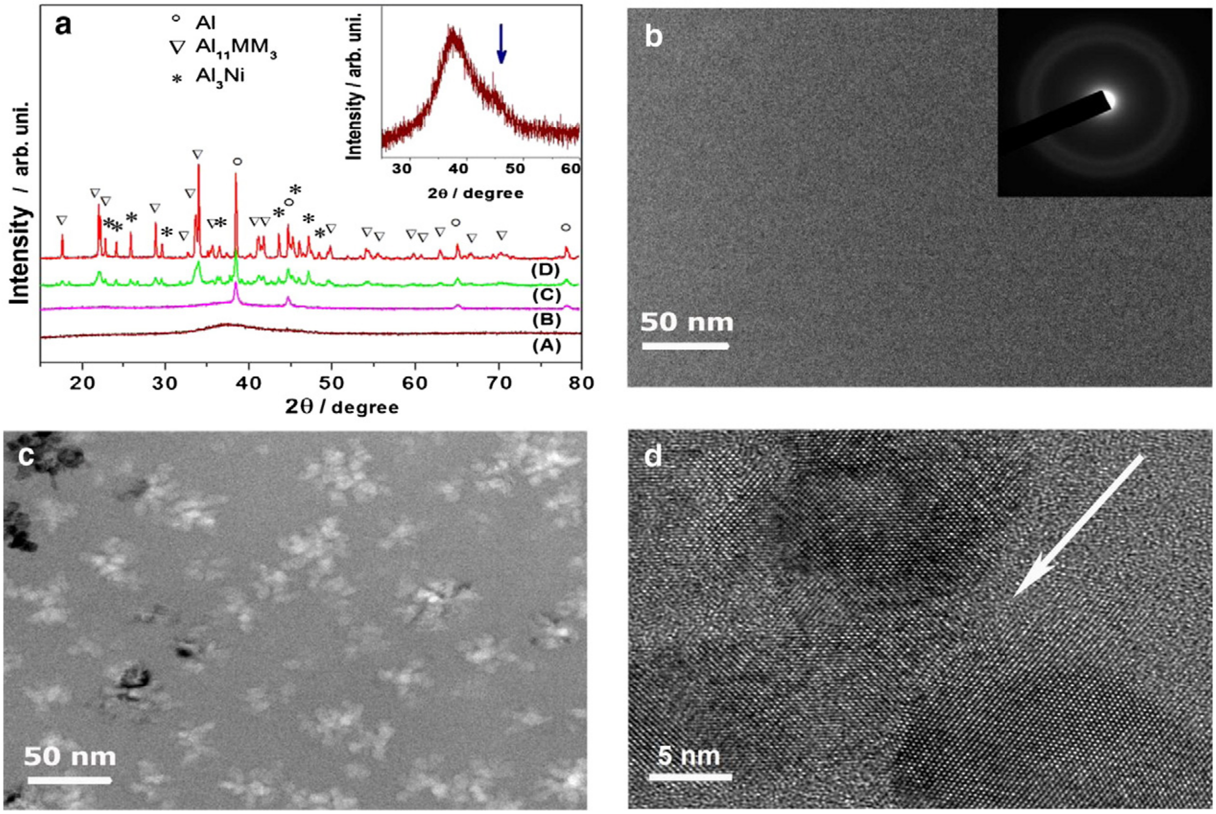

Fig. 2. (a) XRD patterns of $Al_{86}Ni_{10}MM_4$ amorphous alloy after (A) melt spinning (the shoulder at 2θ ≈ 44° is presented in inset), and non-isothermal annealing at temperatures of (B) 553 K, (C) 623 K, and (D) 714 K. (b) HRETM image of the as-quenched alloy. The selected area diffraction pattern determines that the matrix is substatitionally amorphous. (c,d) HRTEM image of the annealed ribbon at 518 K reveals the formation of nanometer-sized aluminum clusters. The twin-like boundary is shown by arrow.

versus $1/T_p$. The slop of the straight lines is proportional to the apparent activation energy, i.e. E = 272 ± 5 kJ/mol.

Fig. 5 shows the normalized values of $z(\alpha)$ and $y(\alpha)$ versus the conversion fraction at various heating rates. The extents of conversion at the maximum values of $z(\alpha)$ and $y(\alpha)$ are reported in Table 1. In order to examine the variation of the activation energy versus the conversion fraction, differential iso-conversional method of Friedman [21] was used (Fig. 6). Three regions can be distinguished. At the early stage (up to $\alpha = 0.2$), the activation energy gradually increased with increasing the conversion fraction but remained almost constant up to $\alpha = 0.8$.

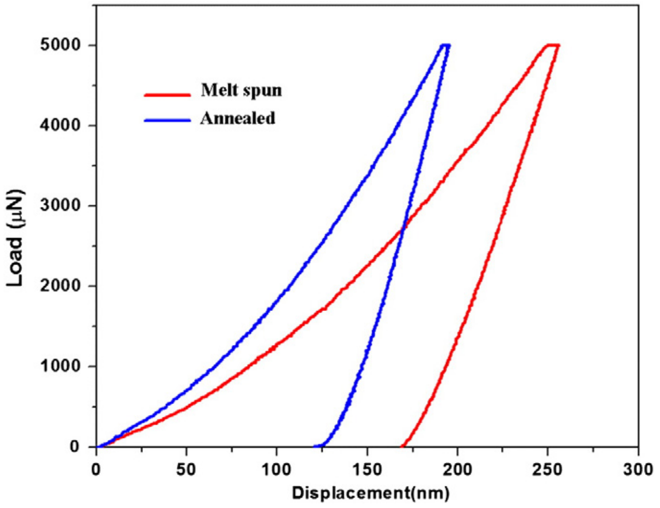

Fig. 3. Typical load-displacement curves of the aluminum alloy at amorphous and annealed states. Annealing was performed at 553 K with a heating rate of 20 K/min.

The average activation energy of the early stage is about 258 ± 5 kJ/mol and reached to a value of 270 ± 6 kJ/mol with the continuation of crystallization within $\alpha = 0.2–0.8$.

4. Discussion

It was shown that the activation energy of the fcc-Al crystallization in amorphous $Al_{86}Ni_{10}MM_4$ alloy is changed with increasing of the conversion fraction (Fig. 6). Although the base line approximation could affect this calculation [26], the lower value of activation energy at the beginning of the crystallization process could be attributed to the presence of quench-in nuclei in the amorphous matrix [27,28] and/or glassy phase separation in the Al-TM-RE systems [29,30]. The shoulder at 2θ ≈ 44° of XRD pattern (see inset in Fig. 2a) could be an evidence of the presence of quench-in nuclei of fcc-Al or Al-rich configuration [31] or a presence of two amorphous phases from glassy phase separation [32]. It is pertinent to point out that sub-nanometer or medium range order (MRO) clusters can be present in the amorphous matrix while they are too small or too little to be observed by TEM or be discerned from XRD [3]. These clusters would operate as preferential sites for nucleation of nanometer-sized aluminum particles without long range diffusion of slow-diffusing solute atoms [4]. Phase separation of the glassy phase to Al-rich and RE-rich regions can also facilitate nucleation of the nanocrystals in the Al-rich amorphous area. Although it is not clear which mechanism is most influential for the formation of the aluminum nanocrystals at the early stage [30], their growth is constrained by the region size and/or gradual compositional change due to diffusion of constituent elements. Consequently, the activation energy of the phase transformation slightly increases with progression of the crystallization. At the late stage of crystallization, the particle spacing of growing nanocrystals decreases; hence, solute build-up

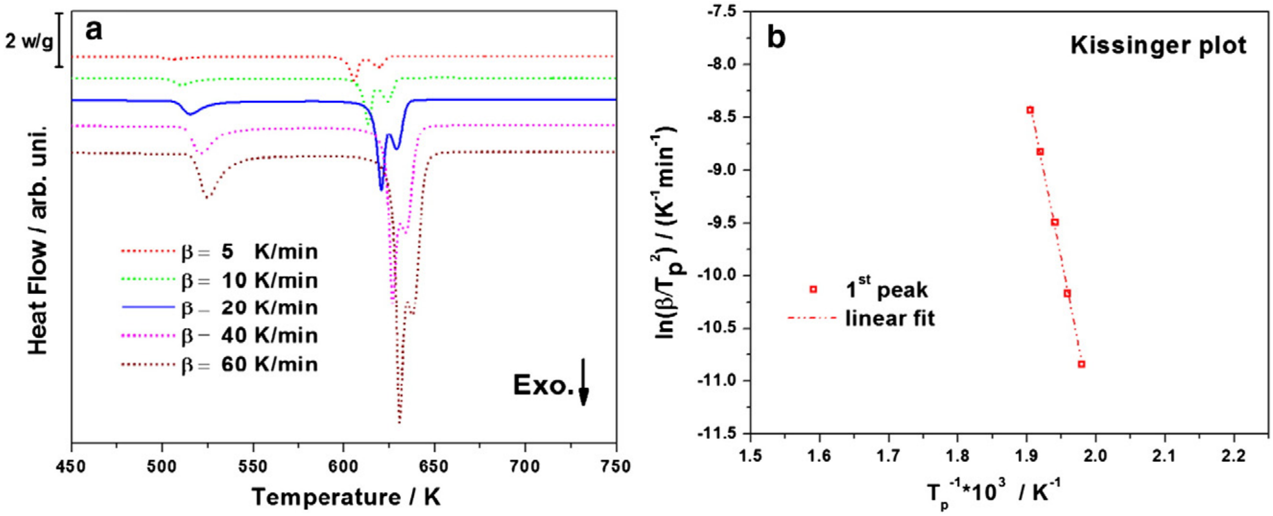

Fig. 4. (a) DSC traces of $Al_{86}Ni_{10}MM_4$ amorphous alloy at various heating rates. (b) Kissinger plot of the first crystallization stage.

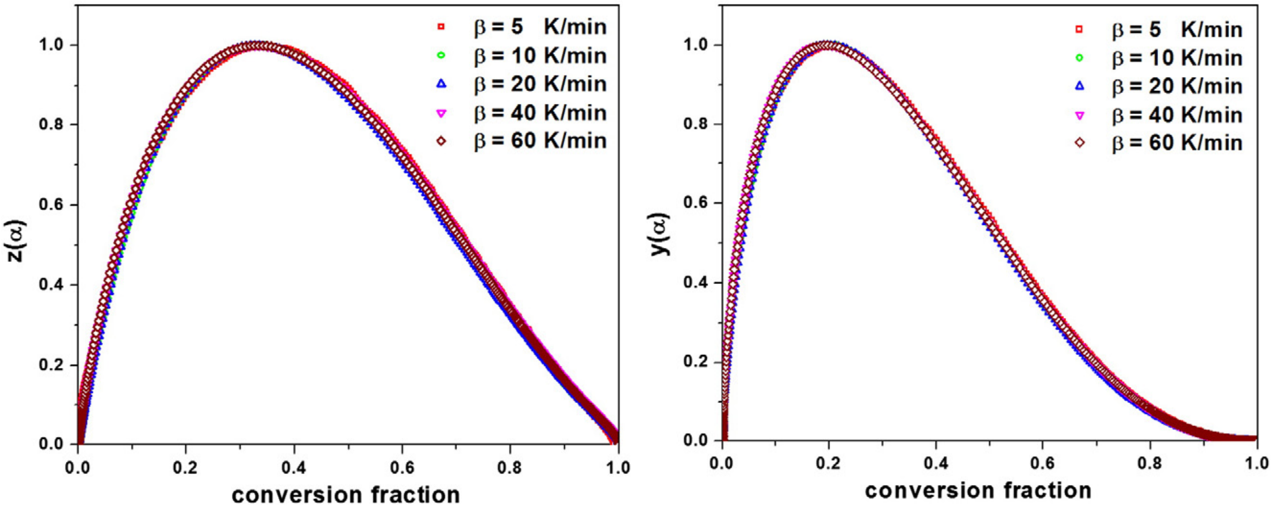

Fig. 5. Normalized values of $z(\alpha)$ and $y(\alpha)$ as a function of conversion fraction at various heating rates.

around the particle is overlapped and further growth of particles is retarded [33].

Non-isothermal crystallization kinetics of crystallization is commonly described by classical Johnson–Mehl–Avrami–Kolmogorov (JMAK) [34] or autocatalytic [16] kinetics model. Malek [26] showed that the maximum value of $z(\alpha)$, i.e. $\alpha_{max,z}$, for JMAK model is 0.632. The lower value indicates that the crystallization process is complex, as shown in Table 1. Therefore, the autocatalytic model was utilized [16]:

$$f(\alpha) = \alpha^{M}(1-\alpha)^{N} \tag{7}$$

Table 1
Values of maximum conversion fractions at different heating rates. The error of calculation was about 0.005 as determined from two closest point in the z(α) and y(α) graphs.

Heating rate (K/min)	$\alpha_{max,z}$	$\alpha_{max,y}$
5	0.343	0.200
10	0.337	0.199
20	0.327	0.196
40	0.335	0.199
60	0.333	0.198

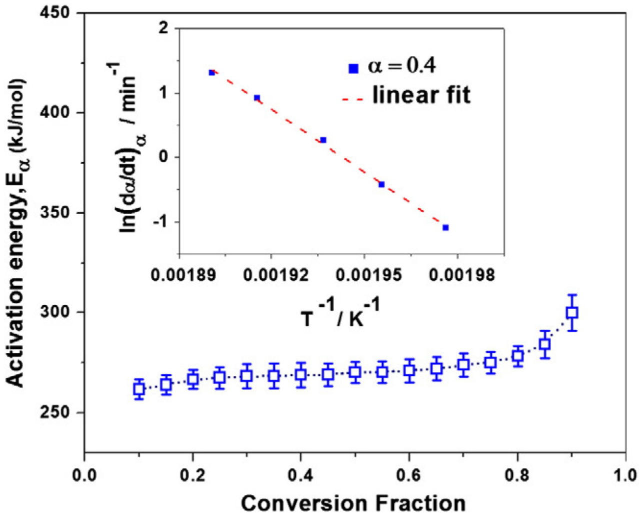

Fig. 6. Variation of activation energy with progression of crystallization in amorphous $Al_{86}Ni_{10}MM_4$ alloy and Friedman plot at $\alpha = 0.4$ (inset).

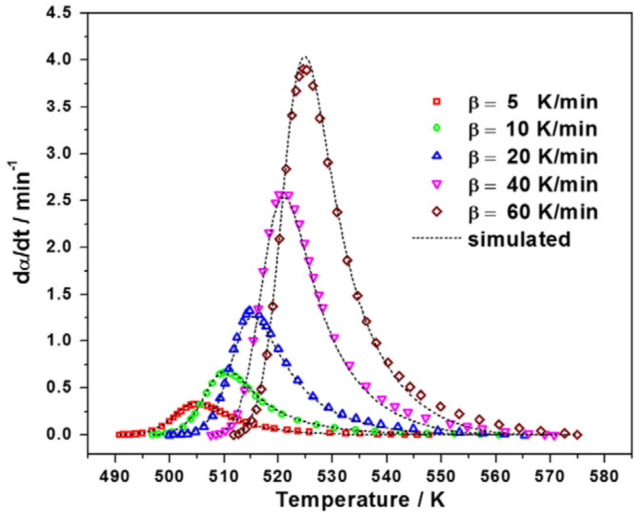

Fig. 7. Reaction rate as a function temperature for the amorphous aluminum alloy. Symbols denote the experimental results obtained from DSC traces and dash lines are predicated values by the autocatalytic model.

where *M* and *N* are kinetic exponents that denote the relative contribution of acceleratory and decay part of crystallization. These exponents can be expressed as a function of $\alpha_{max,y}$ by [23]:

$$\frac{M}{N} = \frac{\alpha_{max,y}}{1-\alpha_{max,y}} \tag{8}$$

Combining Eqs. (1) and (7) yields:

$$\ln\left(\left(\frac{d\alpha}{dt}\right)\exp\left(\frac{E}{RT}\right)\right) = \ln(A) + N\ln(\alpha^{\frac{M}{N}}(1-\alpha)) \tag{9}$$

It should be noted that this model is physically meaningful only for $M < 1$ [16]. The higher *M* value means more important role of conversion fraction on the overall kinetic behavior while higher *N* values reflects the complexity of the crystallization process [26]. Analysis of DSC traces at different heating rates determined the values of the kinetic exponents (Table 2). The average value of *M* and *N* is 0.607 ± 0.015 and 2.441 ± 0.001, respectively. Therefore, the following kinetic equation for the reaction rate of fcc-Al crystallization in amorphous $Al_{86}Ni_{10}MM_4$ alloy can be suggested:

$$\frac{d\alpha}{dt} = 1.54\times10^{28}\exp\left(\frac{-272000}{RT}\right)\alpha^{0.607}(1-\alpha)^{2.441} \qquad \left(\frac{1}{min}\right) \tag{10}$$

In order to evaluate the validity of this equation, the reaction rate as a function of temperature for different heating rates is plotted in Fig. 7. The experimental results are shown in the graph for comparison. A convincing agreement between the experimental results and model predication was attained.

5. Conclusions

Non-isothermal crystallization kinetics of fcc-Al nanocrystals in $Al_{86}Ni_{10}MM_4$ amorphous alloy was studied by calorimetry. The differential iso-conversional model of Friedman and autocatalytic model were utilized. Analysis of DSC traces showed that the crystallization of nano-metric Al crystals is a complex process with an average activation energy value of 272 ± 5 kJ/mol. A change in the value of activation energy was noticed with the progression of the crystallization process due to the presence of quench-in nuclei and/or glassy phase separation as well as solute enrichment and soft impingement during different stages of devitrification. It was shown that non-isothermal crystallization kinetics of fcc-Al precipitation in $Al_{86}Ni_{10}MM_4$ amorphous alloy could quantitatively be described by following rate equation:

$$\frac{d\alpha}{dt} = 1.54\times10^{28}\exp(\frac{-272000}{RT})\alpha^{0.607}(1-\alpha)^{2.441}$$

Table 2
Values of the fitting parameters in the autocatalytic model obtained by using the mean value of the activation energy (272 ± 5 kJ/mol). The maximum standard error of best fitting was calculated by OriginPro 8.5.0 SR1 Software (OriginLab Corporation MA, USA).

Heating rate (K/min)	M ± 0.02	N ± 0.01	ln (A/min) ± 0.01
5	0.615	2.396	64.845
10	0.622	2.496	64.915
20	0.604	2.476	64.971
40	0.601	2.424	64.924
60	0.593	2.411	64.853

References

[1] A. Inoue, Prog. Mater. Sci. 43 (1998) 365–520.
[2] D.V. Louzguine, A.R. Yavari, A. Inoue, J. Non-Cryst. Solids 316 (2003) 225–260.
[3] H. Nitsche, F. Sommer, E.J. Mittemeijer, J. Non-Cryst. Solids 351 (2005) 3760–3771.
[4] M.C. Gao, F. Guo, S.J. Poon, G.J. Shiflet, Mater. Sci. Eng. A 485 (2008) 532–543.
[5] H. Yang, J.Q. Wang, Y. Li, J. Non-Cryst. Solids 354 (2008) 3473–3479.
[6] K.L. Sahoo, M. Wollgarten, J. Haug, J. Banhart, Acta Mater. 53 (2005) 3861–3870.
[7] F. Ye, K. Lu, J. Non-Cryst. Solids 262 (2000) 228–235.
[8] K.L. Sahoo, R. Sahu, J. Non-Cryst. Solids 365 (2013) 33–36.
[9] A. Inoue, K. Ohtera, A.P. Tsai, T. Masumoto, Jpn. J. Appl. Phys. 27 (1988) L479–L482.
[10] Y.H. Kim, A. Inoue, T. Masumoto, Mater. Trans. JIM 31 (1990) 747–749.
[11] Y.H. Kim, K. Hiraga, A. Inoue, T. Matsumoto, H.H. Jo, Mater. Trans. JIM 35 (1994) 293–302.
[12] A. Inoue, Y. Horio, Y.H. Kim, T. matsumoto, Mater. Trans. JIM 33 (1992) 669–674.
[13] K.F. Kelton, T.K. Croat, A.K. Gangopadhyay, L.Q. Xing, A.L. Greer, M. Weyland, X. Li, K. Rajan, J. Non-Cryst. Solids 317 (2003) 71–77.
[14] D. Jacoviks, J. Rodriguez-Viejo, M.T. Clavaguera-Mora, N. Clavaguera, Acta Mater. 52 (2004) 2819.
[15] Y.E. kalay, C. yeager, L.S. Chumbly, M.J. Kramer, I.E. Anderson, J. Non-Cryst. Solids 356 (2010) 1416–1424.
[16] J. Malek, J.M. Criado, J. Sestak, J. Militky, Thermochim. Acta 153 (1989) 429–432.
[17] M.E. Brown, D. Dolimore, A.K. Galwey, vol. 22, Elsevier, Amsterdam, 1980.
[18] J. Malek, Thermochim. Acta 200 (1992) 257–269.
[19] H.E. Kissinger, Anal. Chem. 29 (1957) 1702–1706.
[20] S. Vyazovkin, A.K. Burnham, J.M. Criado, L.A. Pérez-Maqueda, C. Popescu, N. Sbirrazzuoli, Thermochim. Acta 520 (2011) 1–19.
[21] H.L. Friedman, J. Polym. Sci., Part C 6 (1964) 183–195.
[22] P. simon, Thermochim. Acta 520 (2011) 156–157.
[23] R. Svoboda, J. Malek, Thermochim. Acta 526 (2011) 237–251.
[24] G.I. Senum, R.T. Yang, J. Therm. Anal. 11 (1977) 445–447.
[25] M.J. Starink, Int. Mater. Rev. 49 (2004) 191–226.
[26] J. Málek, Thermochim. Acta 355 (2000) 239–253.
[27] D.R. Allen, J.C. Foley, J.H. Perepezko, Acta Mater. 46 (1998) 431–440.
[28] S. Omata, Y. Tanaka, T. Ishida, A. Sato, A. Inoue, Phil. Mag. A. 76 (1997) 387–412.
[29] J. Antonowicz, J. Alloys Compd. 434–435 (2007) 126–130.
[30] D.H. Kim, W.T. Kim, E.S. Park, N. Mattern, J. Eckert, Prog. Mater. Sci. 58 (2013) 1103–1172.
[31] D.V. Louzguine-Luzgin, A. Inoue, J. Alloys Compd. 399 (2005) 78–85.
[32] A.R. Yavar, Acta Metall. 36 (1988) 1863–1872.
[33] D. Jacoviks, J. Rodriguez-Viejo, M.T. Clavaguera-Mora, J. Phys. Condens. Matter 17 (2005) 4897–4910.
[34] J.W. Christian, The Theory of Transformation in Metal and Alloys, Pergamon press, Oxfrod, 1975..